Supplementary Information

Synergistically coupled nickel oxide nanoparticles with single-atom nickel catalysts for high-performance wide-temperature adaptable quasi-solid-state zinc-air batteries

Gargi Dey,[a] Shadab Saifi,[a] Pralay Ranjan Maity,[a] Renna Shakir,[a] Ravi Kumar,[c] D. Bhattacharyya,[c] Jeyakumar Kartikeyan[b] and Arshad Aijaz*[a]

[a]Department of Energy & Human Sciences, Rajiv Gandhi Institute of Petroleum Technology (RGIPT)-Jais, Amethi, Uttar Pradesh-229304, India. Email: aaijaz@rgipt.ac.in

[b]Department of Physics, National Institute of Technology, Durgapur-713209, West Bengal, India.

[c]Atomic & Molecular Physics Division, Bhabha Atomic Research Centre, Mumbai-400094.

Table of Contents

1. Chemicals

All the reagents were purchased commercially and used without further purification. Zinc acetate dihydrate, Nickel acetate tetrahydrate, Acrylamide, Potassium persulphate ($K_2S_2O_8$) and DI water were purchased from Molychem. 2-methylimidazole was purchased from Avra. Cetyltrimethylammonium bromide, Sodium hydroxide pellets, Hydrogen fluoride, Dimethyl sulphoxide, Sulphuric acid (97%), Methanol were purchased from SDFCL. Potassium hydroxide was acquired from Azytus. *t*-Butyl alcohol was purchased from TCI. Nickel (II) acetylacetonate, ethanol, 20 wt% Pt/C, 5% Nafion^{TM} 117 solution, Nickel phthalocyanine, Nickel oxide, Zn foil (0.25mm thickness) (99.99%), Nickel foam, Zinc tetrafluoroborate hydrate were purchased from Sigma-Aldrich. Iridium (IV) oxide powder was purchased from Alfa Aesar. N,N-methylenebisacrylamide (MBAA, Crosslinker) was purchased from SRL (99.5%). ELAT LT 1400 (GDL, Toray TGP-H-06) was purchased by a fuel cell store. High purity Ar (99.999%), 10% Ar/H_2 and O_2 (99.999%) gases were acquired from Sigma-Gases New Delhi and used for high temperature carbonization and electrolyte purging processes.

2. Physicochemical Characterizations

PANalytical diffractometer using Cu Kα source (λ = 1.5405 Å) was used to analyze powder X-ray diffraction (PXRD) with 2°/min scan rate and 0.05 steps. The instrument was operated at 30 kV and a current of 10 mA. N_2 sorption isotherms were recorded by using BELSORP MAX II sorption analyzer at liquid N_2 temperature (77K). Prior to measurements, samples were degassed under vacuum at 120 ºC for 8-12 h. The specific surface area and pore size distribution were evaluated by Brunauer-Emmett-Teller (BET) method and Barrett-Joyner Halenda (BJH) model, respectively. The pore volume was calculated by adsorption amount of N_2 at a relative pressure of 0.99 bar. X-ray photoelectron spectroscopy (XPS) was measured on Thermo Fisher Scientific (K-Alpha) equipment. X-ray photoelectron spectrometer using an Al Kα source (10 kV, 10 mA) equipped with ion source (EX06). UPS was performed on a SPECS Leybold EA11 MCD electron spectrometer and the base pressure in the measurement chamber is in the range of $5*10^{-10}$ mbar. The spectrometer is equipped with a He discharge lamp for UPS (He II at hν = 40.82 eV). EPR spectra were conducted on a benchtop spectrometer Bruker EMXnano with x band. Scanning electron microscopic (SEM) images were acquired using JEOL (JXA-8230) at 20 kV. 200 kV Talos F200S G2 transmission electron microscope combined with column energy dispersive X-ray spectrometer (EDS) and a CMOS Camera 4K x 4K detector were used for Transmission Electron Microscopy (TEM) measurements. High Resolution high-angle annular dark-field scanning transmission electron microscopy (HAADF-STEM) measurement was taken on a JEM-ARM200F instrument at 200 kV. PERKIN ELMER OPTIMA 5300 DV ICP-OES was used for the determination of

metal contents in samples. Raman spectroscopy measurements were carried out on the Princeton instruments (Acton spectra pro-2500i) with the help of 532 nm DPSS Laser (laser quantum gem with a power of 50 mW). The stretchable properties of gel electrolyte were investigated using Tensile machine. The freezing point of the gel electrolyte was characterized by a DSC1 (Mettler Toledo) under the N_2 atmosphere with a cooling rate of 5 °C min^{-1}. The XAS measurements have been carried out at the Energy-Scanning EXAFS beamline (BL-9) at the Indus-2 Synchrotron Source (2.5 GeV, 100 mA) at Raja Ramanna Centre for Advanced Technology (RRCAT), Indore, India[1,2]. This beamline operates in the energy range of 4 KeV to 25 KeV. The beamline optics consists of a Rh/Pt coated collimating meridional cylindrical mirror and the collimated beam reflected by the mirror is monochromatized by a Si(111) (2d = 6.2709 Å) based double crystal monochromator (DCM). The second crystal of DCM is a sagittal cylinder used for horizontal focusing while a Rh/Pt coated bendable post mirror facing down is used for vertical focusing of the beam at the sample position. Rejection of the higher harmonics content in the X-ray beam is performed by detuning the second crystal of DCM. In the present case, XAS measurements have been performed in the transmission mode for the Ni standards and for sample in the fluorescence mode.

References

1. A. K. Poswal, A. Agrawal, A. K. Yadav, C. Nayak, S. Basu, S. R. Kane, C. K. Garg, D. Bhattachryya, S. N. Jha and N. K. Sahoo, *AIP Conference Proceedings* 1591 (1), 649-651 (2014).

2. S. Basu, C. Nayak, A. K. Yadav, A. Agrawal, A. K. Poswal, D. Bhattacharyya, S. N. Jha and N. K. Sahoo, *Journal of Physics: Conference Series* 493 (1), 012032 (2014).

d-band center calculations: The d-band center was calculated according to Eq. S1. Surface valence band photoemission spectra were corrected by subtracting the Shirley background. For the accurate comparison of all valence-band spectra, the upper level of integration of background subtraction was set at the 10.0 eV bonding energy position throughout all valence-band spectra. [1-3]

$$\mu = \frac{\int N(\varepsilon)\varepsilon \, d\varepsilon}{\int N(\varepsilon) d\varepsilon} \qquad \ldots\ldots\ldots (S1)$$

where $N(\varepsilon)$ is the DOS. μ is the center of d-band. ε is bonding energy.

1. Hofmann, T.; Yu, T. H.; Folse, M.; Weinhardt, L.; Bär, M.; Zhang, Y.; Merinov, B. V.; Myers, D. J.; Goddard, W. A.; Heske, C., Using Photoelectron Spectroscopy and Quantum Mechanics to Determine D-Band Energies of Metals for Catalytic Applications. *J. Phys. Chem. C.*, **2012**, *116*, 24016-24026.

2. Chen, Z., et al., Tailoring the D-Band Centers Enables Co_4N Nanosheets to Be Highly Active for Hydrogen Evolution Catalysis. *Angew. Chem. Int. Ed.*, **2018**, *57*, 5076-5080.

3. Lou, Y., et al., Promoting Effects of In_2O_3 on Co_3O_4 for Co Oxidation: Tuning O_2 Activation and Co Adsorption Strength Simultaneously. *ACS Catal.*, **2014**, *4*, 4143-4152.

3. Electrochemical Measurements

The electrochemical measurements for HER, OER, and ORR were performed by using a traditional 3-electrode setup connected with VSP 128 bi-potentiostat (BioLogic). The reference, working, and counter electrodes were Hg/HgO, glassy carbon, and graphitic rod electrodes (graphitic rod for ORR, Pt mesh for OER), respectively. All potentials were normalized to values in relation to the reversible hydrogen electrode. To make catalyst ink, 5 mg of catalyst was mixed with DI water (490 µl), ethanol (490 µl), and Nafion 5% (20 µl) then sonicated for 20 minutes at room temperature. Afterwards, a specific volume of catalyst ink was dropped onto the pre-cleaned surface of the working electrode, equivalent to 0.210 mg cm^{-2}. The electrodes were held to dry in the air prior to testing of electrochemical activity. Before performing linear sweep voltammograms (LSVs) (5 mV s^{-1}) at room temperature, electrodes were preconditioned by taking repeating cyclic voltammograms (CVs) in desired potential range. All OER were tested in Ar-saturated solution of 1 M KOH. The ORR measurements were tested in 0.1M KOH at 5 mV sec^{-1} in O_2-saturated solution. For ORR, LSVs were recorded at different electrode rotation speeds (100-2500 rpm). The Tafel slope values for OER extracted from the kinetic region of performed LSVs. The electrochemical active surface area (ECSA) was calculated by taking CV scans at different scan rates in a non-Faradaic region. The obtained current density is assumed to be due to charging in the non-Faradaic region. Then, the difference in current density variation (J_a-J_c) vs RHE were plotted against the scan rate. C_{dl} was collected from its slope. Finally, ECSA was obtained by dividing the slope value by specific capacitance (C_s), generally C_s value is 0.035 mF cm^{-2} was used for catalyst surface. Electrochemical impedance spectroscopy (EIS) was performed in the frequency range from 1,00,000 to 0.01 Hz at 5 mV s^{-1} scan rate. EIS fitting circuit model provides the R_s (series resistance) and R_{ct} (charge transfer resistance) values, which are analyzed by in-built Biologic software.

TOF calculations for OER:

TOF for OER was calculated using the catalyst-modified disc electrode (RRDE), subject to a potential ramp over a specified potential range in which OER occurs considerably, while the ring electrode was held at a constant cathodic potential adequate to reduce the O_2 developed from the disc electrode. The used equation for TOF calculation is:

$$TOF = i_R / A \times F \times n \times N_{CL} \times \Gamma \quad \text{..... (S2)}$$

Where, i_R, A, F, n, N_{CL}, and Γ, represent the ring current, area of the electrode, Faraday constant, the number of electrons transferred to produced one molecule of the product, collection efficiency of RRDE

electrode, and surface concentration or accurate number of active sites catalyzing the reaction (m^{-2}), respectively.

Faradaic efficiency calculations for OER:

FE for OER was calculated via RRDE electrode using formula,

$$F.\ E. = I_r/N \times I_d \quad \text{..... (S3)}$$

Where, I_r and I_d stand for ring current and disc current, respectively. N is the current collection efficiency for Pt ring (0.41).

Quasi-solid-state ZABs measurements:

Quasi-solid-state Zn-air battery was assembled using PAM modified hydrogel solid electrolyte. The as-prepared hydrogels were immersed in the 6 M KOH + 0.2 M Zn $(OAc)_2 \cdot 6H_2O$ electrolyte for 72 h before use. A clean Zn foil (0.2 mm thickness) was used as an anode. The air electrode (cathode) was made by dropping catalyst ink onto a flexible GDL with loading of 1.5 mg cm^{-2}. The battery was tested at different temperatures ranging from -70 ºC to 70 ºC. All battery data tested with with VSP 128 bi-potentiostat (BioLogic).

Electrolytic cell measurements:

Two electrode water electrolysis device was assembled using NiO/Ni-SACs/mNC1000 as OER catalyst and Pt/C as HER catalyst. A homogeneous ink of NiO/Ni-SACs/mNC1000 was uniformly coated on nickel foam to generate an electrode with 1.2 mg cm^{-2} catalyst loading. The electrochemical activity was tested by taking voltammograms in Ar-saturated solution at 5 mV s^{-1}.

4. Binding energy calculations with Gaussian:

Density functional theory (DFT) was performed for binding energy calculations of the gel electrolytes using Gaussian 16 software. We used B3LYP function with basis set 6-311+g (d,p). First, the geometries were optimized and then counterpoise corrected energy were calculated. The binding energy E_b can be calculated according to the following equation:

$$E_b = E_{total} - \sum E_{component} \quad \text{(S4)}$$

where E_{total} is the total energy, $E_{component}$ is the energy of each component. The higher absolute value of E_b indicates stronger interactions.

5. Density Functional Theory calculations:

Spin-polarized DFT calculations were conducted using the Vienna Ab initio Simulation Package (VASP) code.[1] The projector augmented wave (PAW) scheme[2,3] was employed to describe all atoms, and the exchange-correlation effects were corrected using generalized gradient approximations (GGA) with PBE functions.[4] A consistent energy cutoff of 500 eV was applied for all calculations. The electronic

convergence criterion was set at 10^{-6} eV, and the final residual forces on each atom in optimized structures were maintained below 0.01 eV/Å. To prevent interactions between periodic images of the NiN_4-graphene monolayer, a minimum vacuum length of 20 Å was maintained in the z-direction. For the geometry optimization of the NiN_4-graphene monolayer, a Monkhorst-Pack 2×2×1 k-point grid was utilized. The Gibbs free energy changes for each electron transfer reaction were calculated using the computational standard hydrogen electrode (CHE) model, developed by Nørskov et al[4] defined as:

$$\Delta G = \Delta H + \Delta ZPE - T\Delta S + G_{pH}$$

Here, ΔH, T, ΔS, and ΔZPE denote the change in enthalpy from the DFT calculation, temperature, change in entropy, and change in zero-point energy of the reaction, respectively. G_{pH} is the correction of the free energy due to variations in the concentration of H^+ and is defined as:[5]

$$G_{pH} = k_B T \times \ln[H^+]$$

In this study, we considered pH = 0, and the temperature parameter for each calculation step was set to 298.15 K. The entropy for free gas molecules were obtained from the NIST database, while those for the adsorbed species were computed from the vibrational frequencies of the adsorbed intermediates. Therefore, only vibrational entropy was considered for the calculation of change in entropy (ΔS) for the adsorbed species. The mechanisms underlying the oxygen evolution reaction (OER) in both acidic and basic medium can be described as follows:

$$H_2O + e^- \rightarrow OH^* + H^+ + e^-$$

$$OH^* \rightarrow O^* + H_2O + (H^+ + e^-)$$

$$O^* + H_2O \rightarrow OOH^* + H^+ + e^-$$

$$OOH^* \rightarrow * + O_2 + H^+ + e^-$$

1. Kresse, G.; Furthmüller, J. Efficient iterative schemes for ab initio total-energy calculations using a plane-wave basis set. *Phys. Rev. B* **1996**, *54*, 11169–11186.

2. Blöchl, P. E. Projector augmented-wave method. *Phys. Rev. B* **1994**, *50*, 17953–17979.

3. Kresse, G.; Joubert, D. From ultrasoft pseudopotentials to the projector augmented-wave method. *Phys. Rev. B* **1999**, *59*, 1758–1775.

4. Perdew, J. P.; Burke, K.; Ernzerhof, M. Generalized Gradient Approximation Made Simple. *Phys. Rev. Lett.* **1996**, *77*, 3865– 3868.

5. Nørskov, J. K.; Rossmeisl, J.; Logadottir, A.; Lindqvist, L.; Kitchin, J. R.; Bligaard, T.;Jónsson, H. Origin of the overpotential for oxygen reduction at a fuel-cell cathode. *J.Phys. Chem. B* **2004**, *108*, 17886–17892.

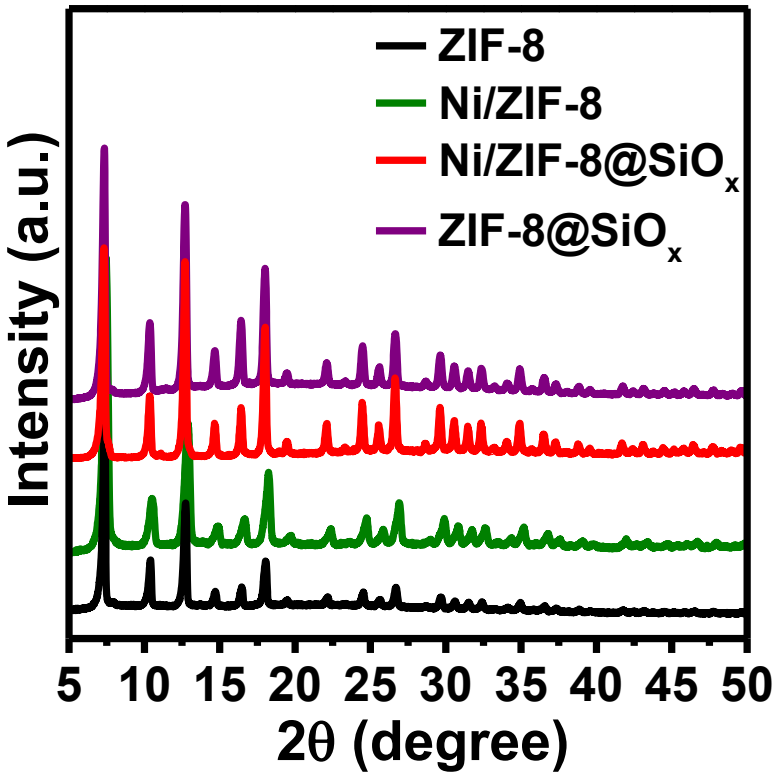

Fig. S1 PXRD patterns of ZIF-8, Ni/ZIF-8, Ni/ZIF-8@SiO_x, and ZIF-8@SiO_x.

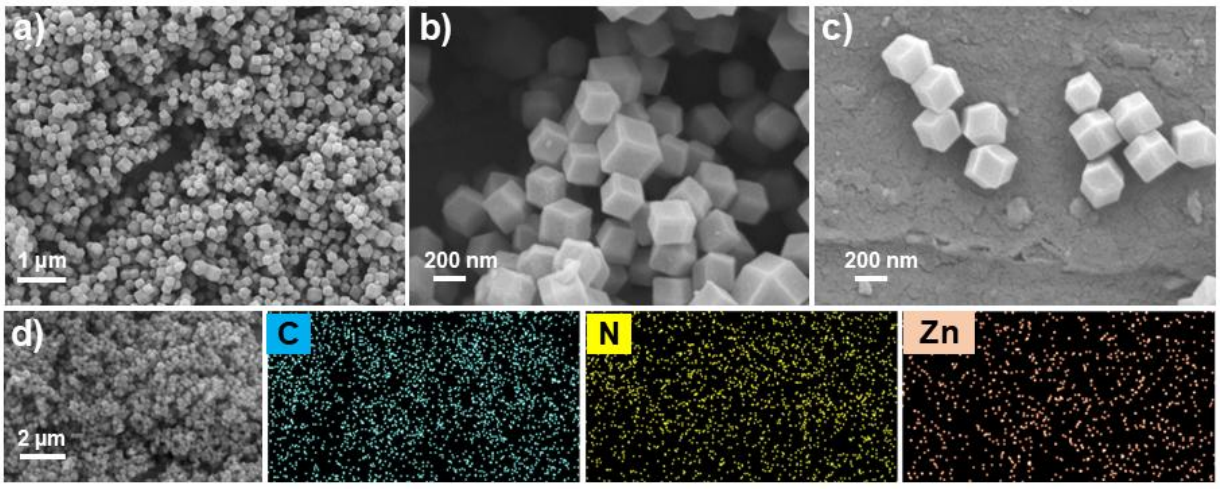

Fig. S2 a-c) SEM images of ZIF-8 at different scale bars. d) SEM image with corresponding EDS elemental mappings of ZIF-8.

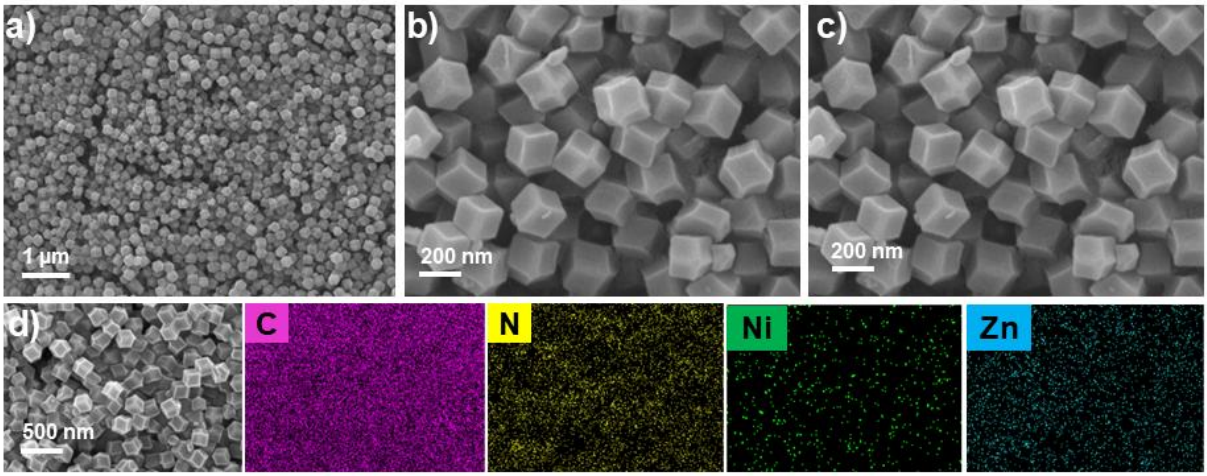

Fig. S3 a-c) SEM images of Ni/ZIF-8 at different scale bars. d) SEM image with corresponding EDS elemental mappings of Ni/ZIF-8.

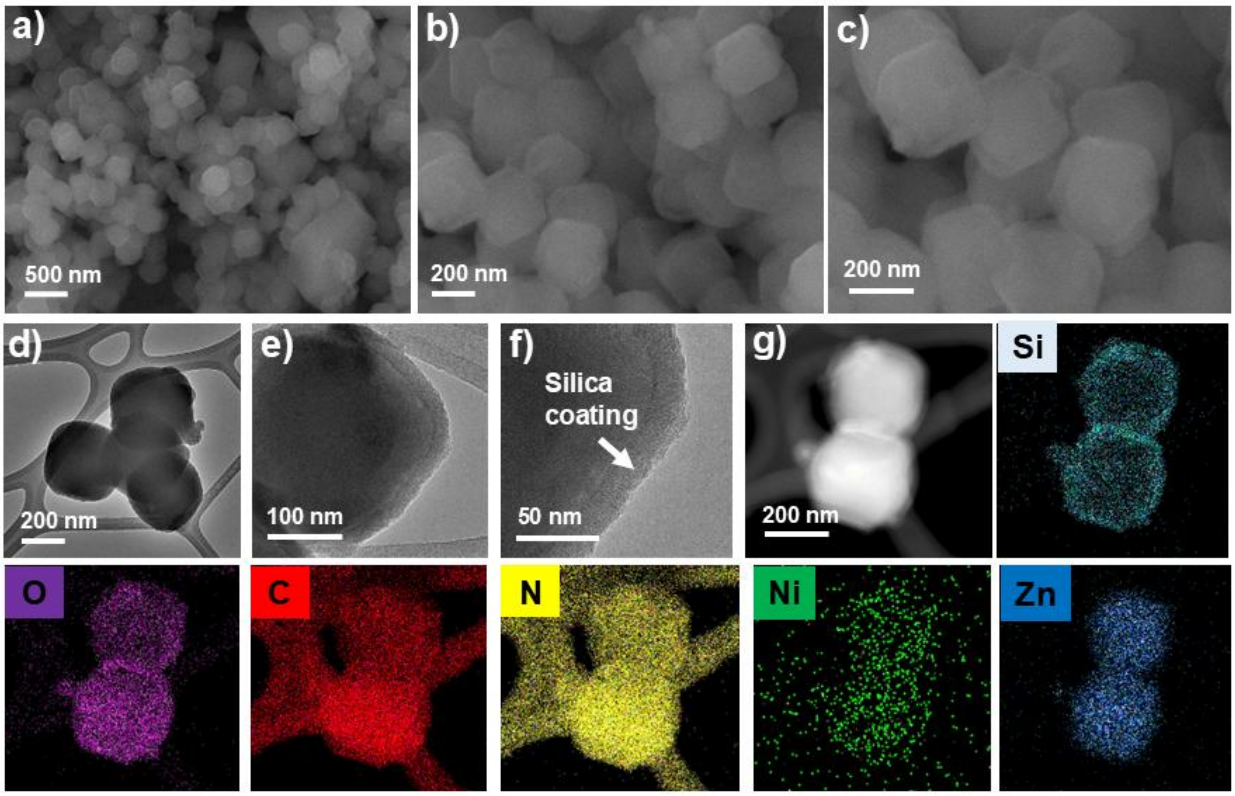

Fig. S4 a-c) SEM images of Ni/ZIF-8@SiO_x at different scale bars. d-f) TEM images of Ni/ZIF-8@SiO_x. g) HAADF-STEM image and its corresponding EDX elemental mapping of Silicon (cyan), Oxygen (purple), Carbon (red), Nitrogen (yellow), Nickel (green), Zinc (blue).

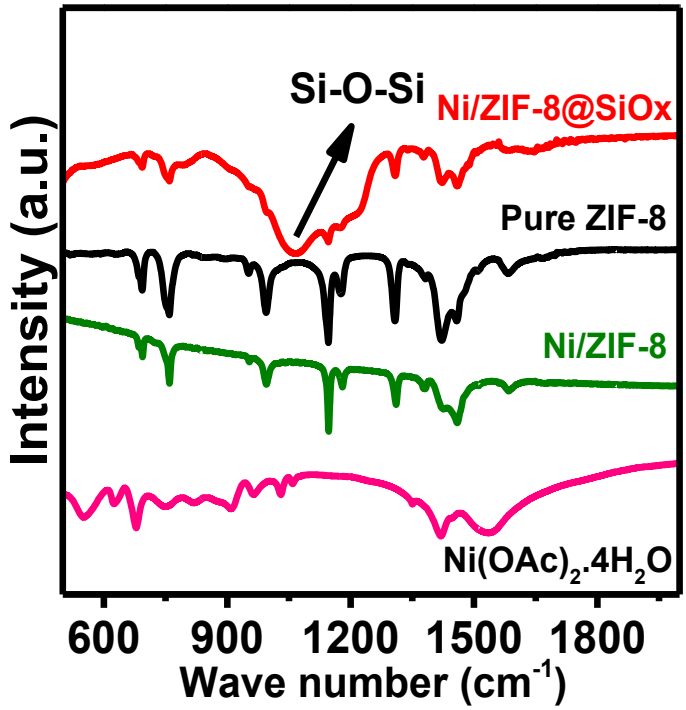

Fig. S5 FT-IR spectra of $Ni(OAc)_2.4H_2O$, ZIF-8, Ni/ZIF-8 and Ni/ZIF-8@SiO_x.

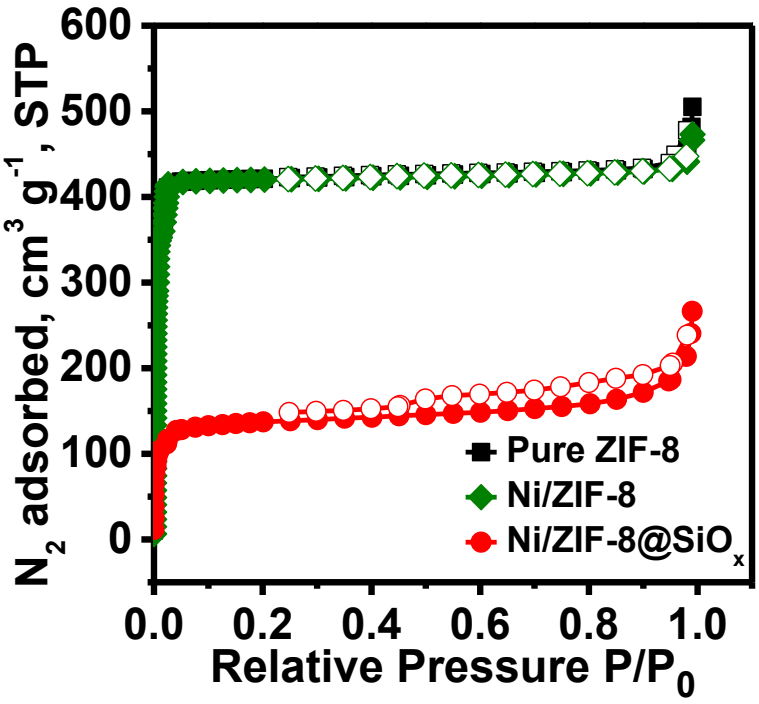

Fig. S6 N_2 adsorption-desorption isotherms for ZIF-8, Ni/ZIF-8 and Ni/ZIF-8@SiO_x.

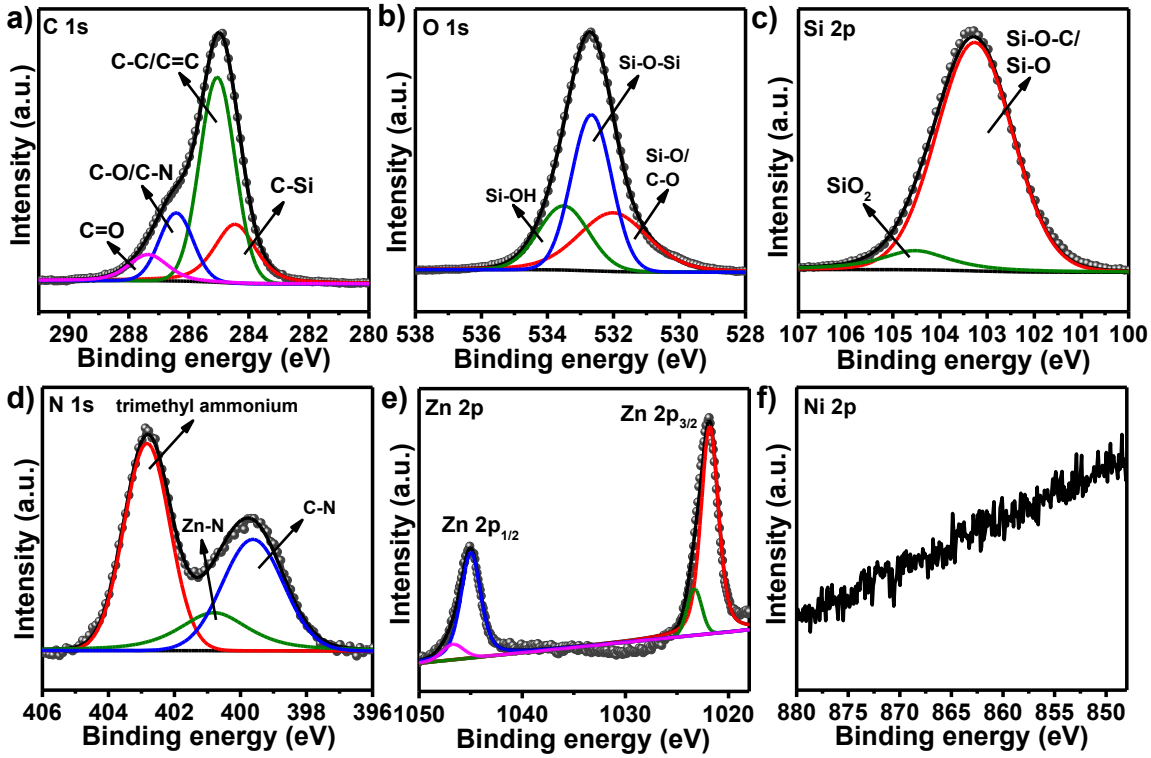

Fig. S7 High-resolution XPS spectra of C 1s, O 1s, Si 2p, N 1s, Zn 2p, Ni 2p acquired from Ni/ZIF-8@SiO_x.

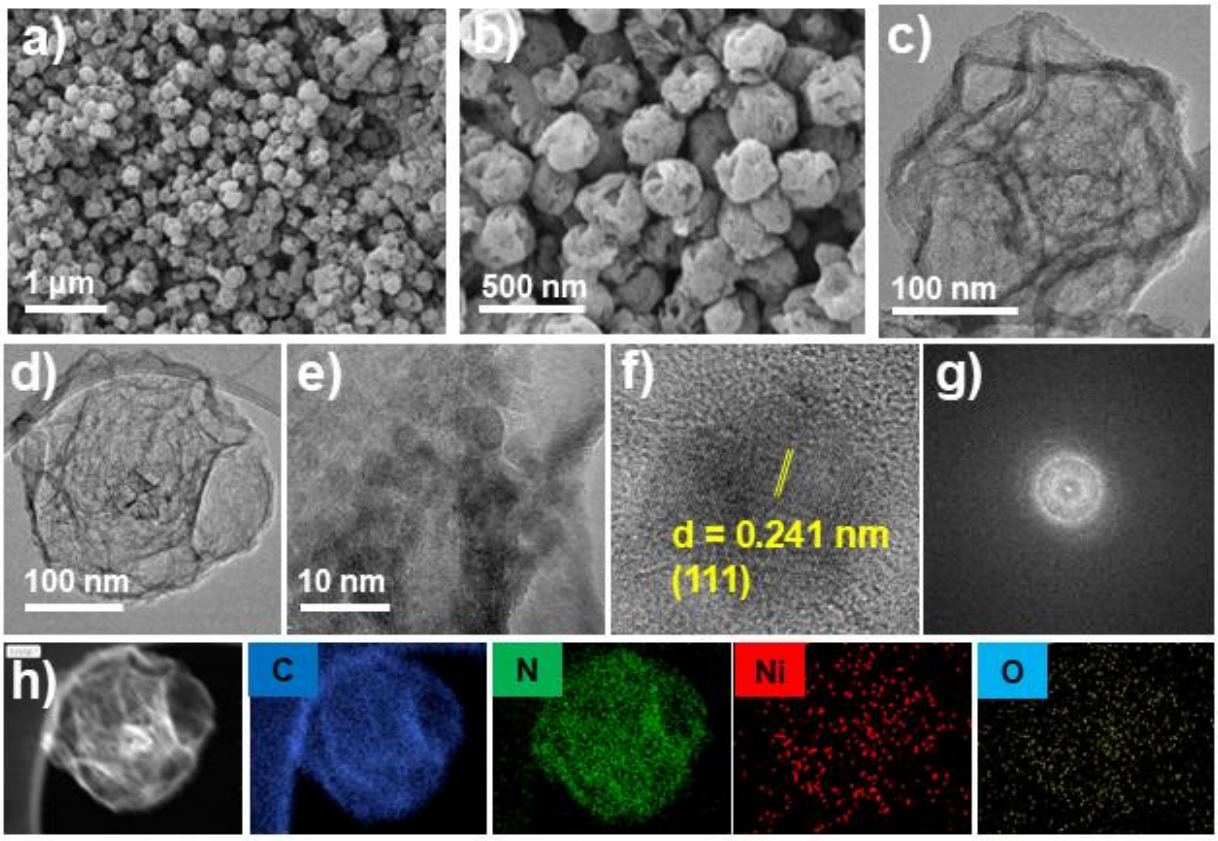

Fig. S8 a-b) SEM images of NiO/Ni-SACs/mNC900 at different scale bars. c-d) TEM images of NiO/Ni-SACs/mNC900. e) HR-TEM images where small NiO nanoclusters distributed over carbon. f) d-spacing calculations from corresponding fringes of NiO nanoclusters. g) SAED pattern of NiO/Ni-SACs/mNC900. h) HAADF-STEM image and its corresponding EDX elemental mapping of Carbon (blue), Nitrogen (green), Nickel (red) and Oxygen (yellow).

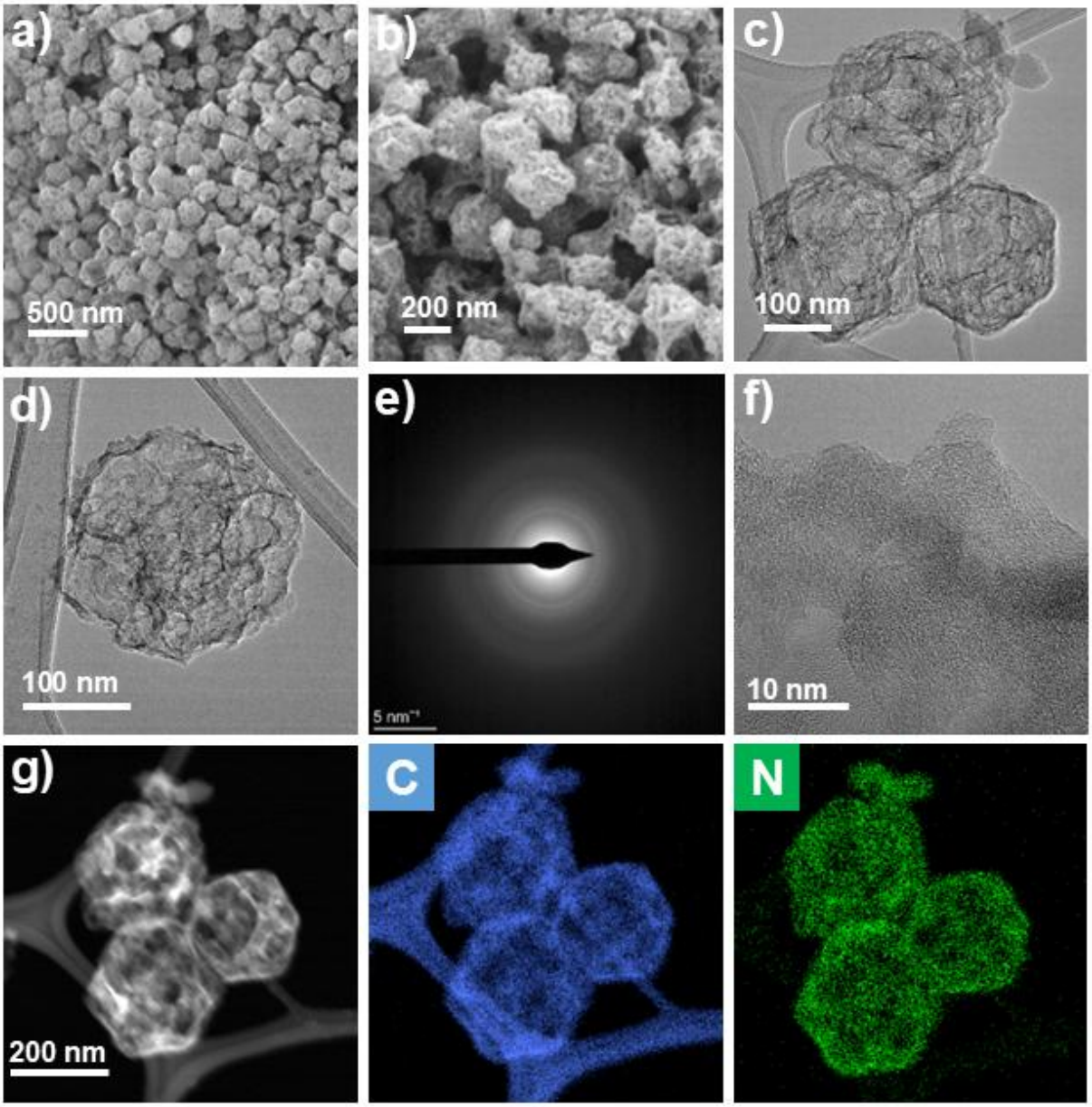

Fig. S9 a-b) SEM images of mNC1000 at different scale bars. c-d) TEM images of mNC1000. e) SAED pattern of mNC1000. f) HR-TEM image where no metallic particles or clusters are present. g) HAADF-STEM image and its corresponding EDX elemental mapping of Carbon (blue) and Nitrogen (green).

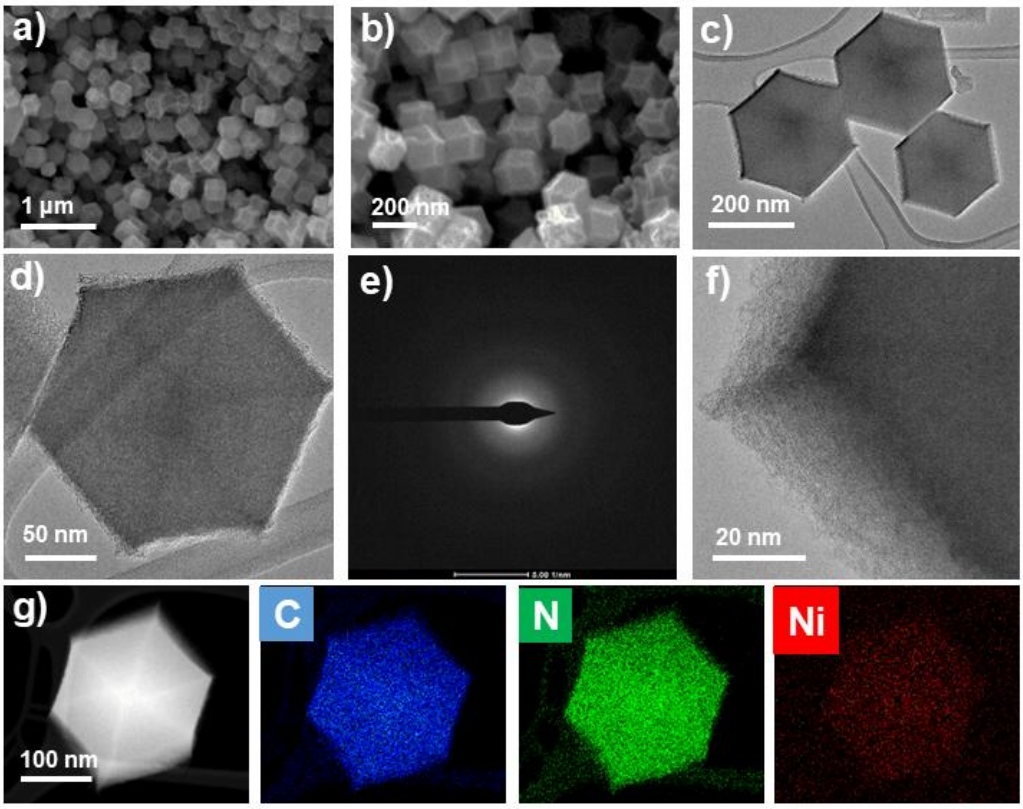

Fig. S10 a-b) SEM images of Ni-SACs/NC1000 at different scale bars. c-d) TEM images of Ni-SACs/NC1000. e) SAED pattern of Ni-SACs/NC1000. f) HR-TEM image where no metallic particles or clusters are present. g) HAADF-STEM image and its corresponding EDX elemental mapping of Carbon (blue), Nitrogen (green) and Nickel (Red).

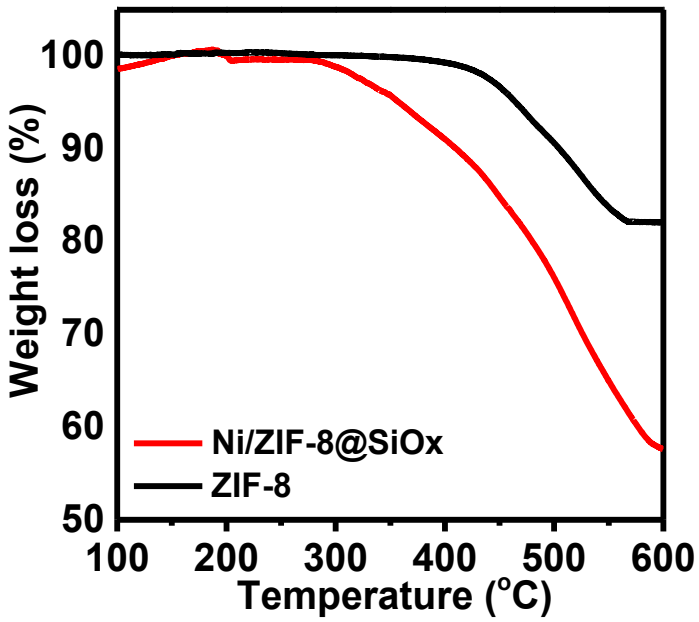

Fig. S11 TGA of ZIF-8 and Ni/ZIF-8@SiOx at a ramp rate of 10 °C min^{-1} under N_2 flow.

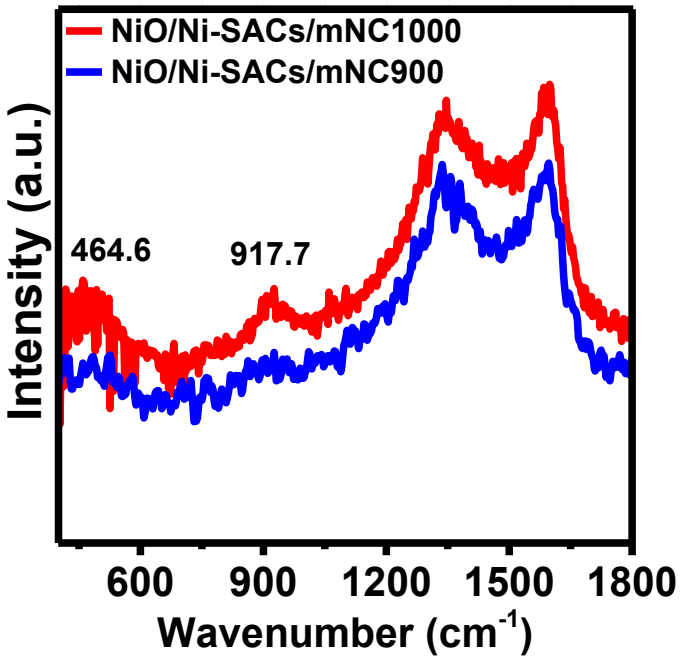

Fig. S12 Raman spectra of NiO/Ni-SACs/mNC1000 and NiO/Ni-SACs/mNC900.

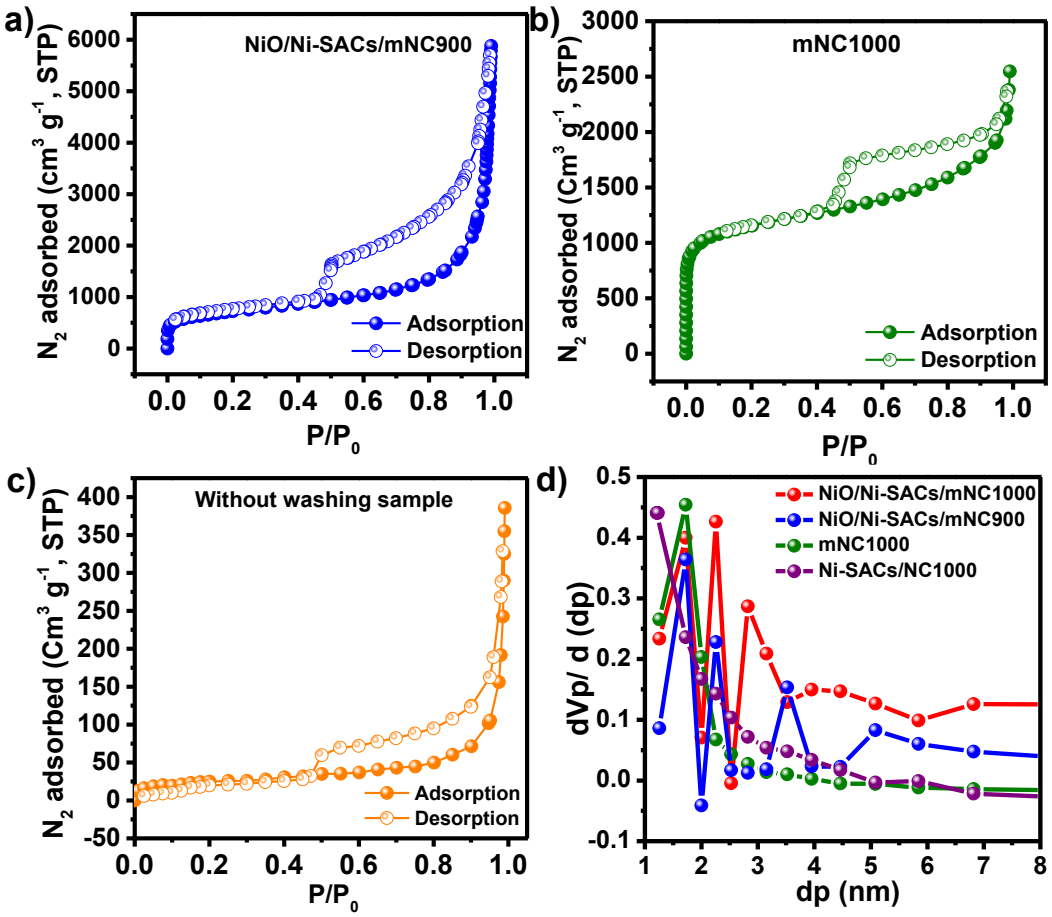

Fig. S13 a-c) N_2 adsorption-desorption isotherms of NiO/Ni-SACs/mNC900, mNC1000 & without washed sample of NiO/Ni-SACs/mNC1000, respectively. d) BJH analysis for pore size distribution of NiO/Ni-SACs/mNC1000 and supporting catalysts.

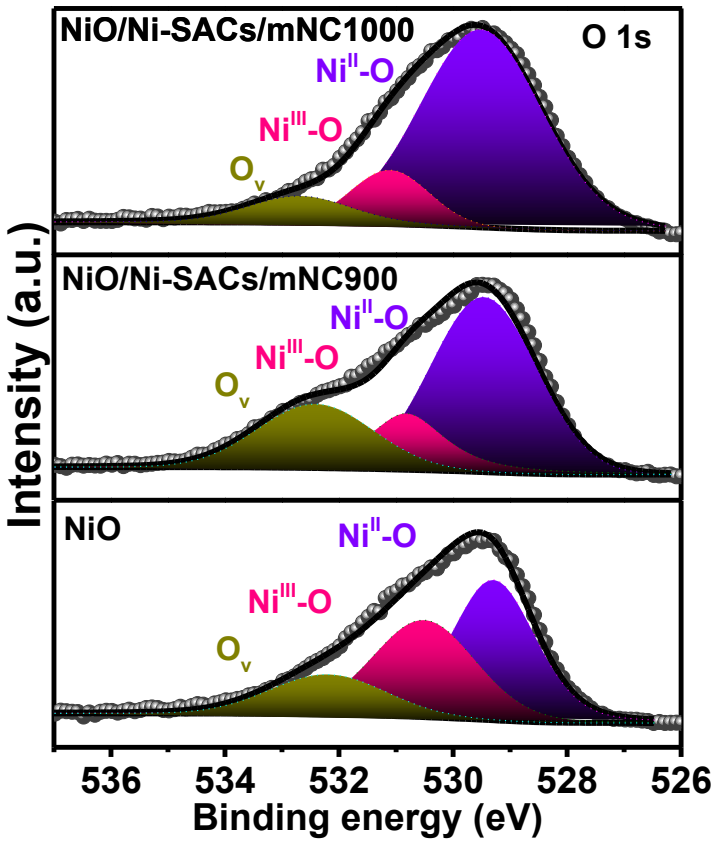

Fig. S14 Comparison of O 1s XPS spectra of NiO/Ni-SACs/mNC1000 and NiO/Ni-SACs/mNC900 with pristine NiO nanoparticles.

Table S1 Bond length, coordination number and disorder factors obtained by EXAFS fitting measured at Ni K- edge.

Path	Parameter	Main catalyst
Ni K edge		
Ni-N	**R (Å) (1.88)**	**1.85 ± 0.01**
	N (4)	**4 ± 0.04**
	σ^2	**0.0032 ± 0.001**

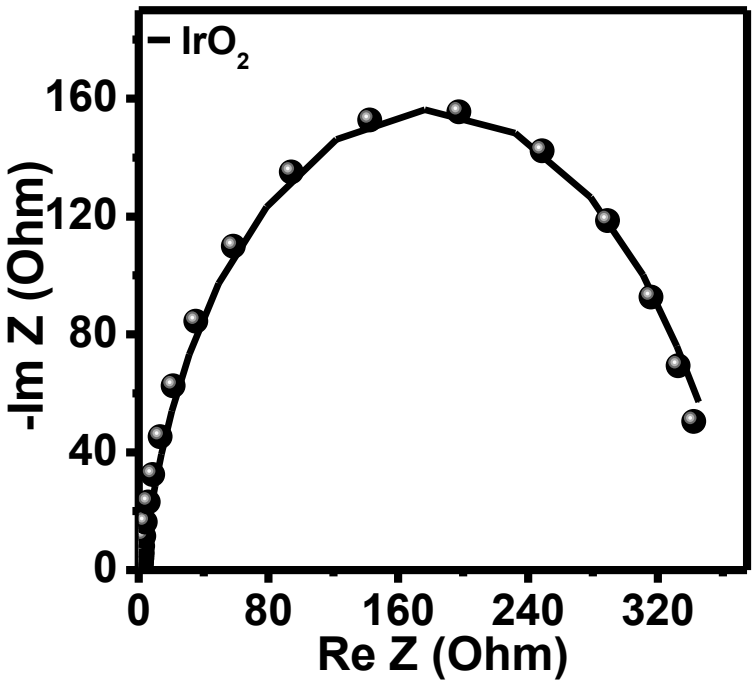

Fig. S15 Nyquist plots of IrO_2 in 1 M KOH for OER.

Table S2 Equivalent electrical circuit model & its corresponding fitting parameters used for the OER kinetics.

Circuit	Catalyst Name	Fitting parameters			
		R_s (Ω)	CPE	a2	R_{ct} (Ω)
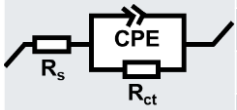	NiO/Ni-SACs/mNC1000	1.35	0.01	0.88	1.54
	NiO/Ni-SACs/mNC900	1.38	0.01	0.86	1.76
	Ni-SACs/NC1000	1.39	0.008	0.89	3.21
	mNC1000	1.4	0.0145	0.895	3.79
	IrO_2	1.39	0.0016	0.92	338.39

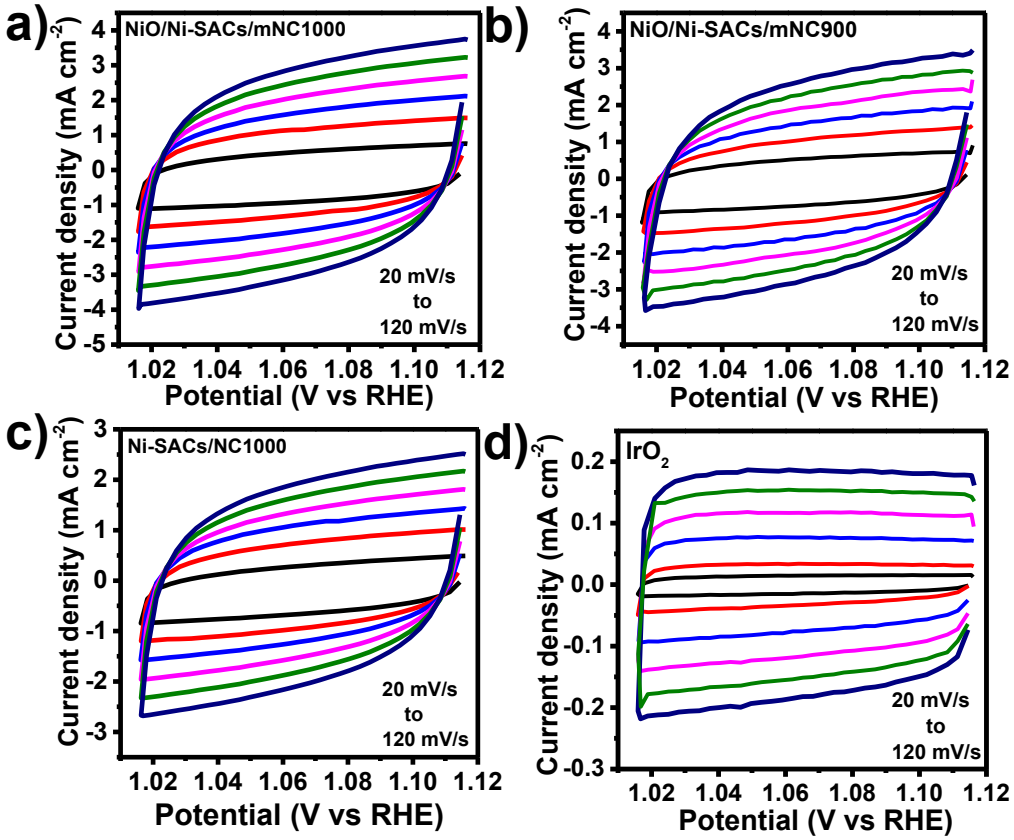

Fig. S16 CV curves of a) NiO/Ni-SACs/mNC1000, b) NiO/Ni-SACs/mNC900, c) Ni-SACs/NC1000 and d) IrO_2 in a potential range of 1.028 to 1.128 V vs RHE at different scan rates in 1 M KOH.

Table S3 Calculated d-band center from density of states plot for different catalytic sites.

Catalyst system	d-band center (Average)
NiN_4	-2.6256
NiN_4-NiO	-2.2878
NiO (111)	-2.3831

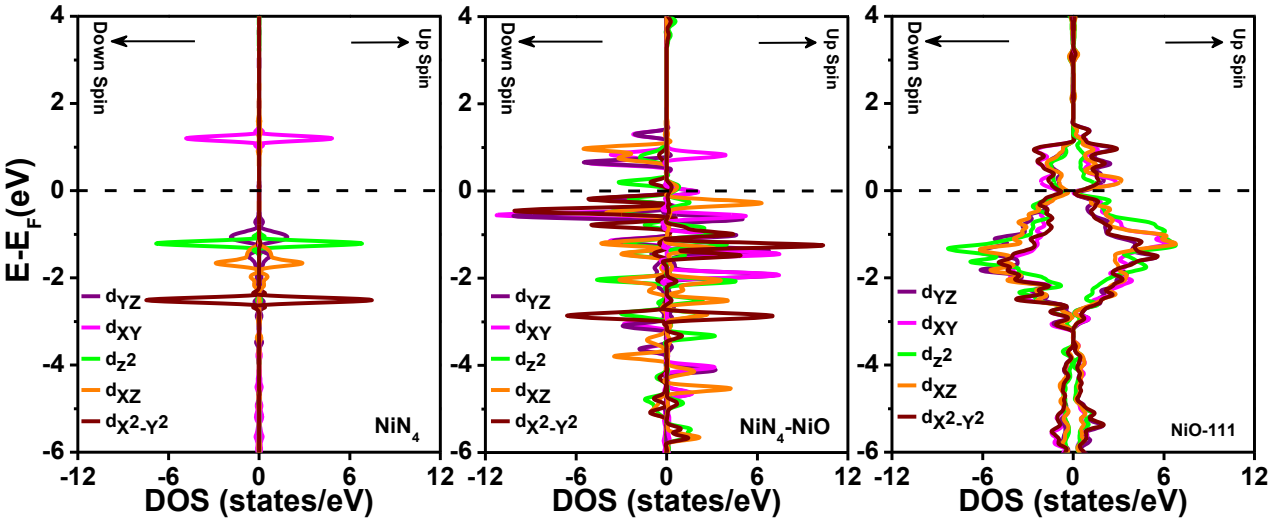

Fig. S17 PDOS of NiN_4, NiN_4-NiO, and NiO (111). Fermi energy (E_F) is at zero.

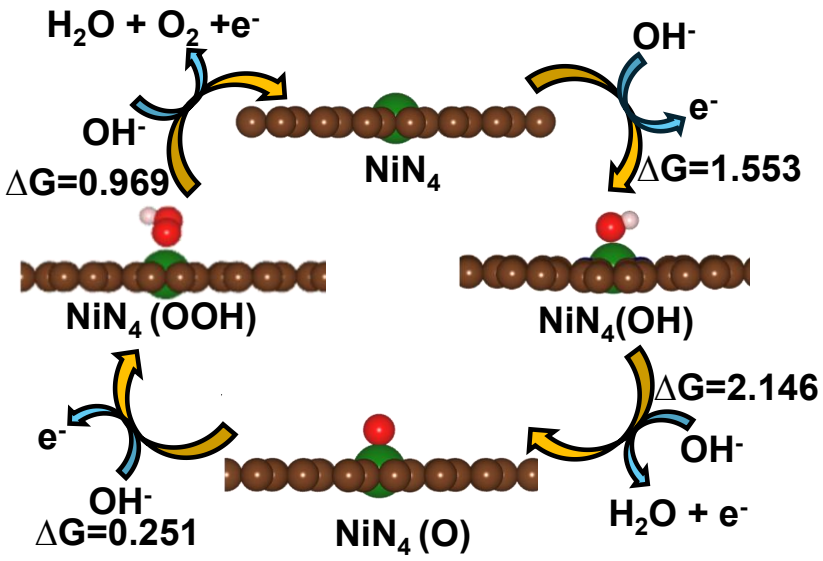

Fig. S18 OER mechanism with optimised structure for intermediates adsorbed on Single-Ni-atom site of NiN_4.

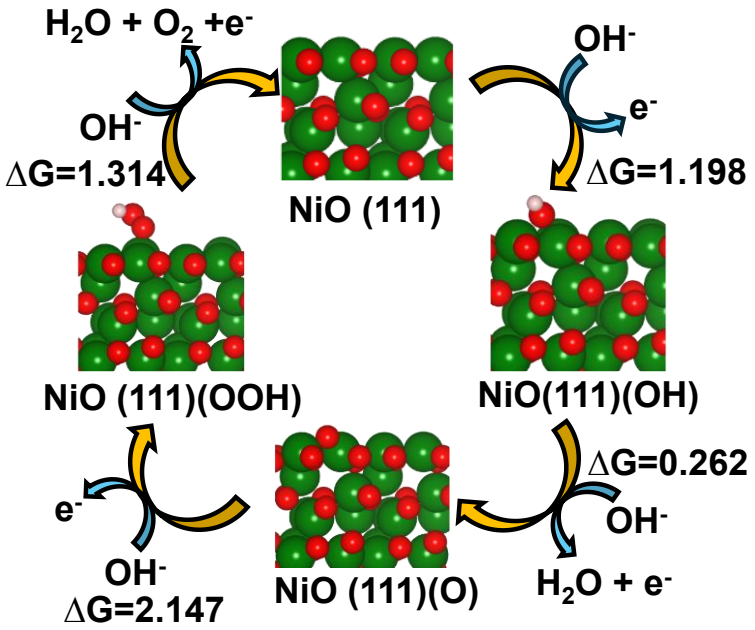

Fig. S19 OER mechanism with optimised structure for intermediates adsorbed on NiO (111).

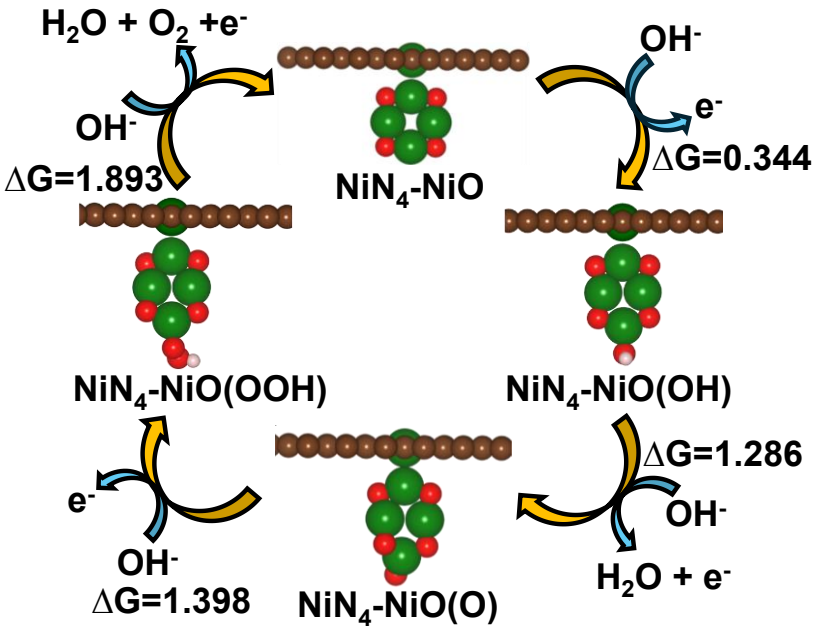

Fig. S20 OER mechanism with optimised structure for intermediates adsorbed on NiO site of NiN_4-NiO.

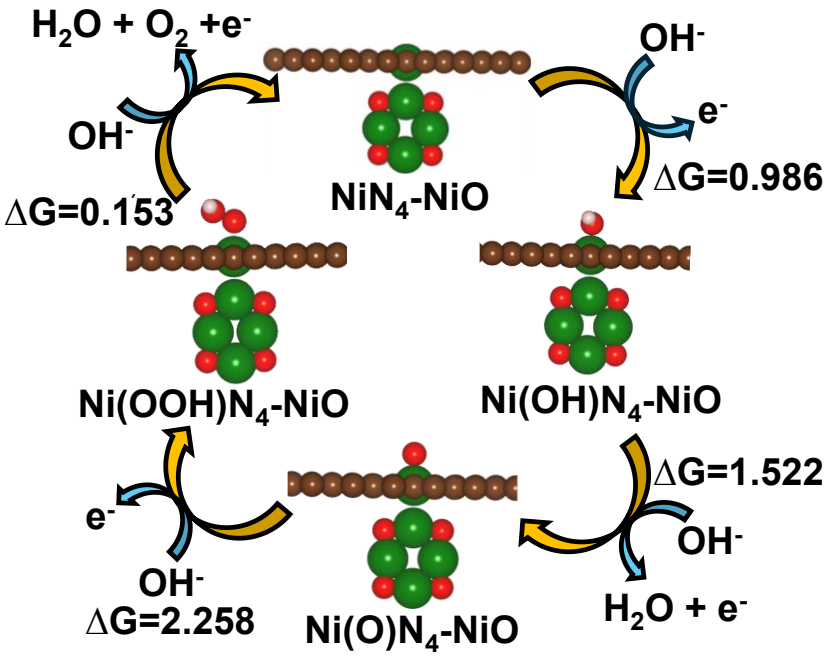

Fig. S21 OER mechanism with optimised structure for intermediates adsorbed on Single-Ni-atom site of NiN_4-NiO.

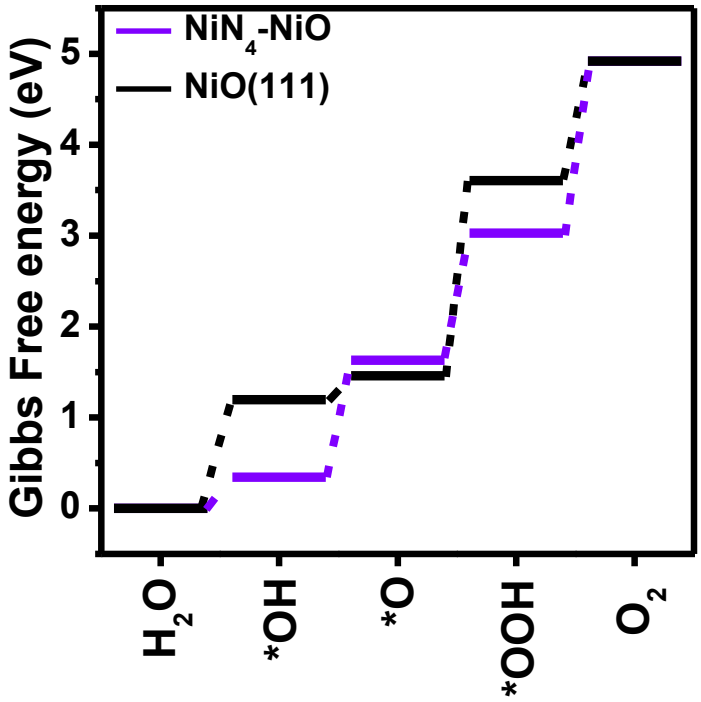

Fig. S22 Comparison of calculated free energy for OER on NiO site of NiN_4-NiO and NiO (111).

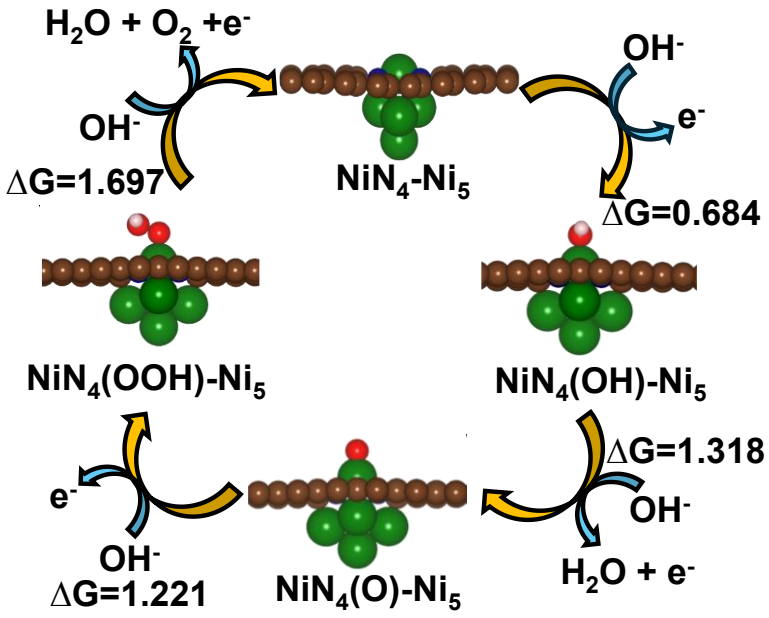

Fig. S23 OER reaction mechanism with optimised structure for intermediates adsorbed on Single-Ni-atom site of NiN_4-Ni_5.

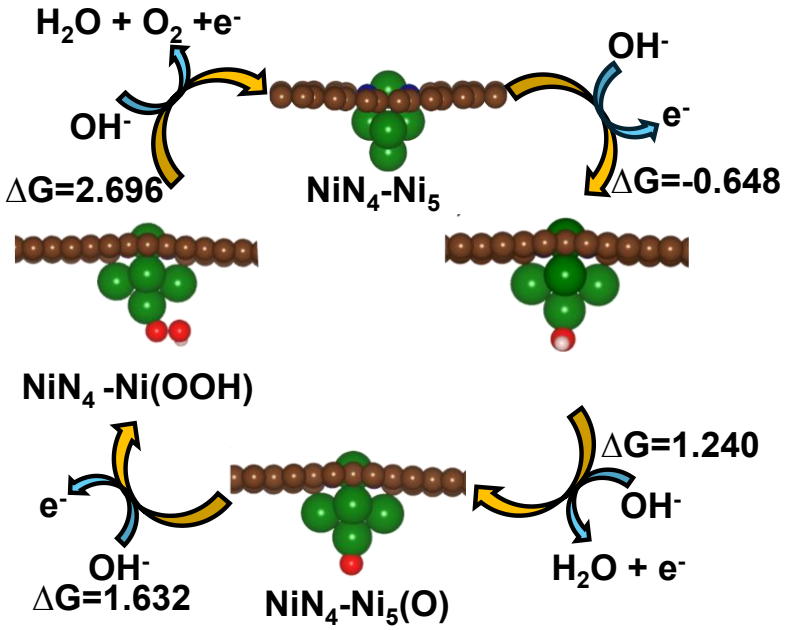

Fig. S24 OER reaction mechanism with optimised structure for intermediates adsorbed on Ni clusters of NiN_4-Ni_5.

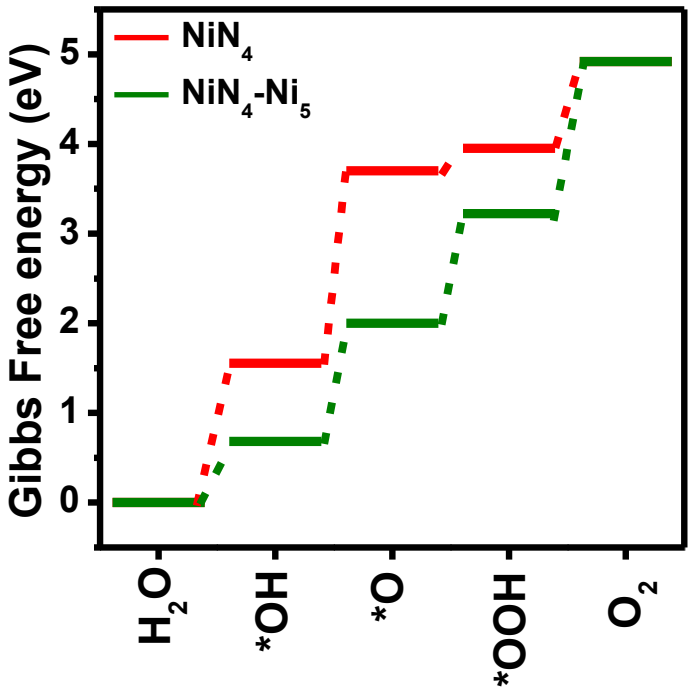

Fig. S25 Comparison of calculated free energy for OER on Ni-single-atom site of NiN_4-Ni_5 and NiN_4.

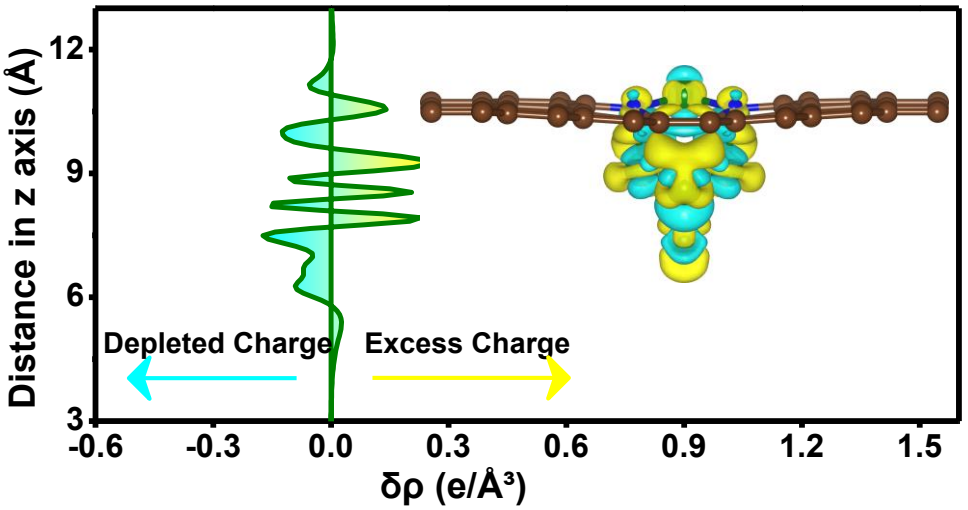

Fig. S26 Differential charge density plots of NiN_4-Ni_5. Isosurface levels are set at ±0.004 $e^{-}/Å^3$. Yellow represents the charge buildup region, and cyan represents the charge depletion region.

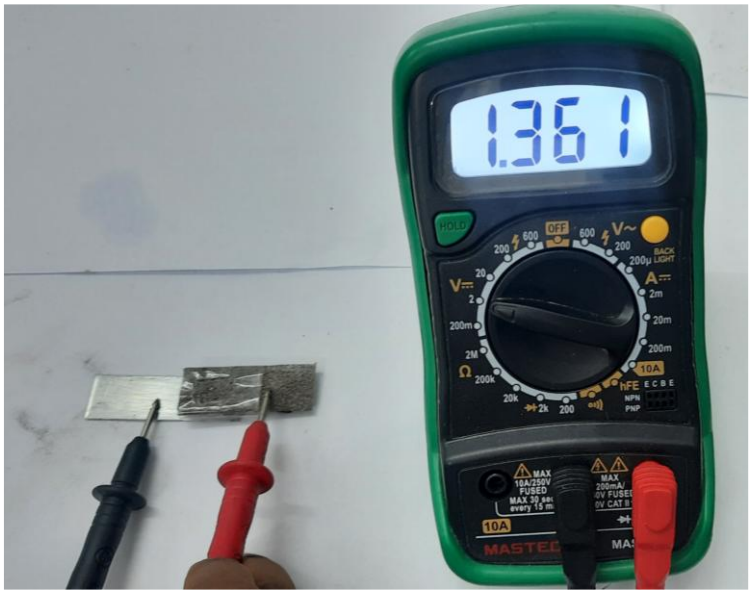

Fig. S27 Photograph displaying measured open-circuit-voltage of 1.361 V for solid state ZAB using PAM-h electrolyte for NiO/Ni-SACs/mNC1000.

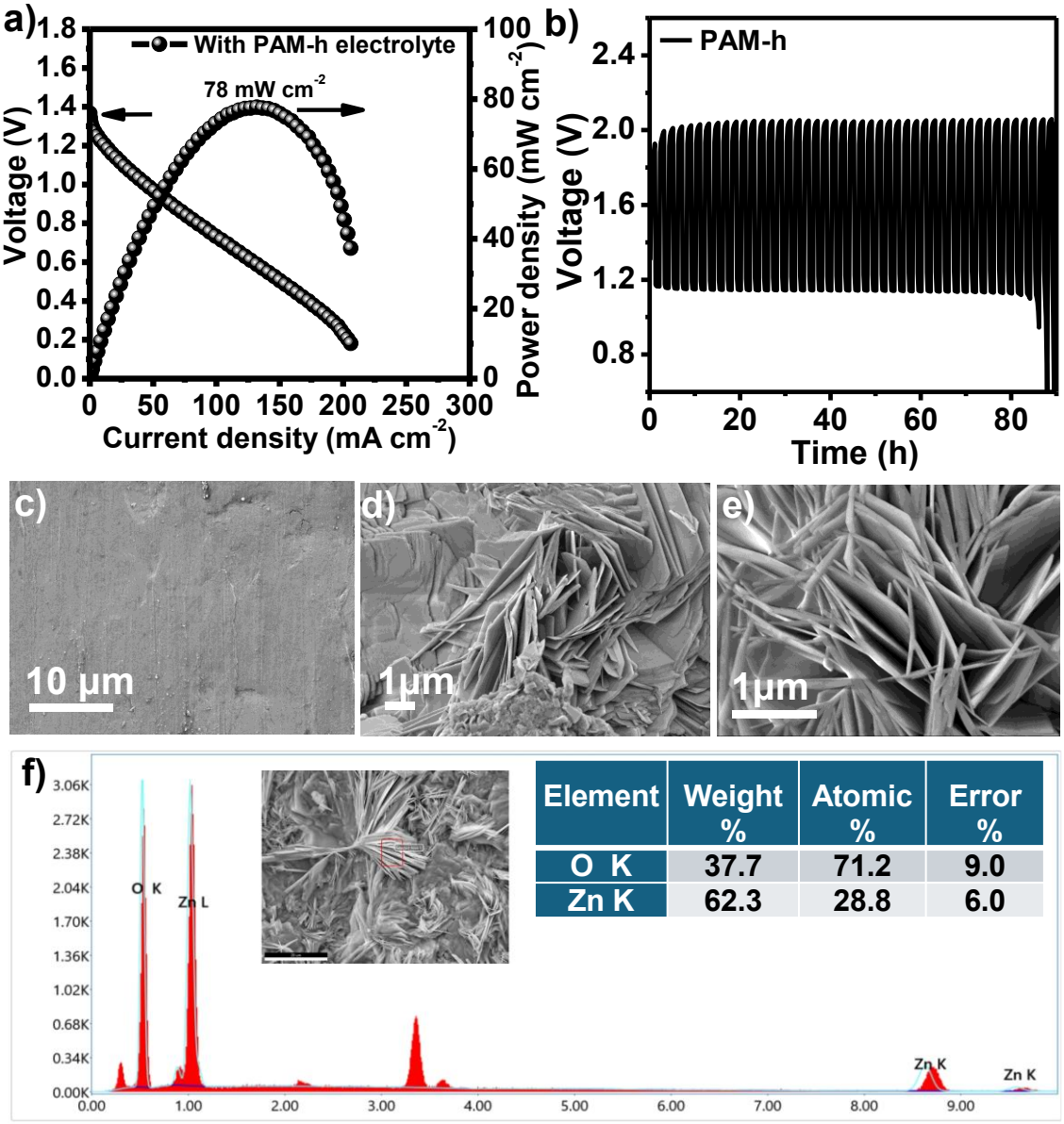

Element	Weight %	Atomic %	Error %
O K	37.7	71.2	9.0
Zn K	62.3	28.8	6.0

Fig. S28 a) polarization curve and b) charging discharging curve at 10 mA cm^{-2} with PAM-h gel electrolyte and NiO/Ni-SACs/mNC1000 for solid state ZAB. c) SEM image of fresh Zn plate. d)-e) SEM images of Zn plate after battery testing with PAM-h gel electrolyte. f) The corresponding EDS results of the cycled Zn plate.

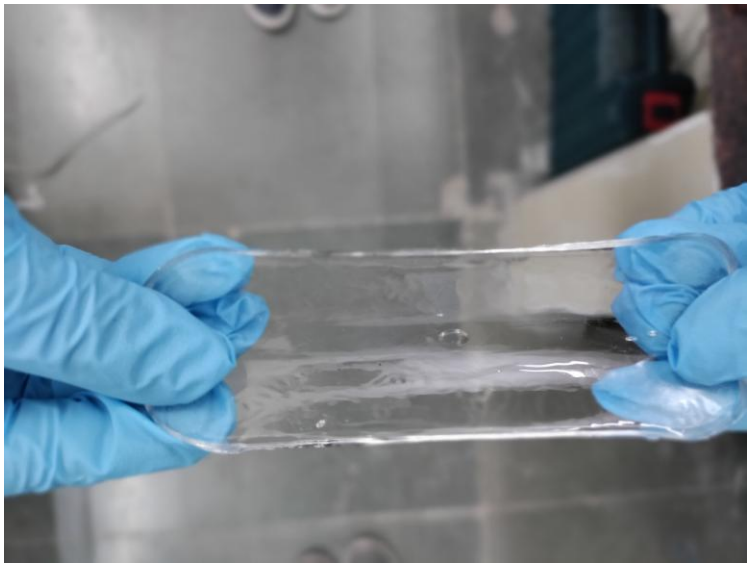

Fig. S29 Photograph of PAM-zdh electrolyte.

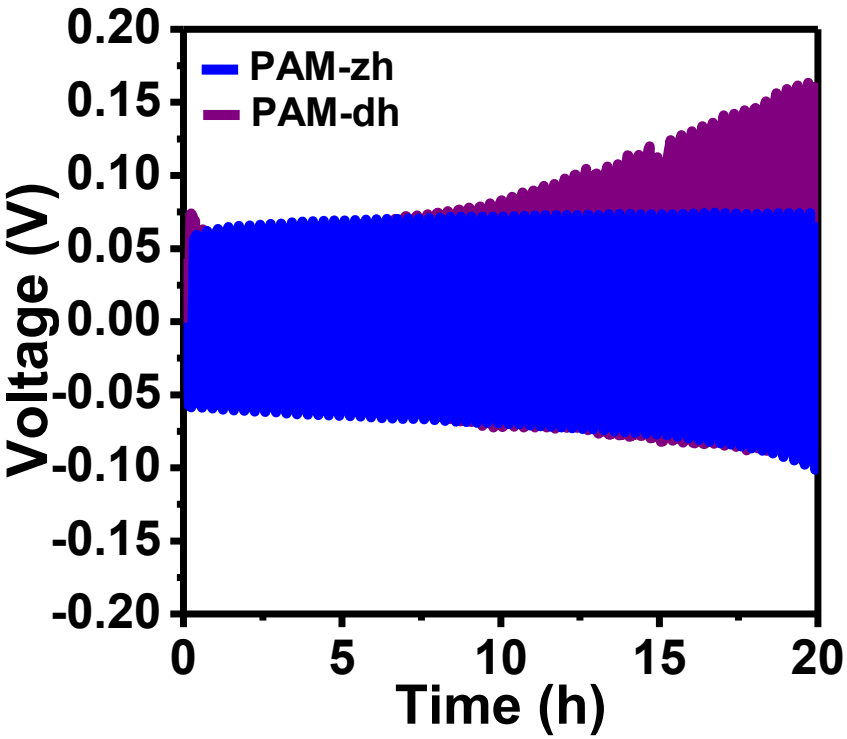

Fig. S30 Cycling performance of the symmetric Zn ||Zn cells employing PAM-zh & PAM-dh hydrogel electrolyte at 5 mA cm^{-2}.

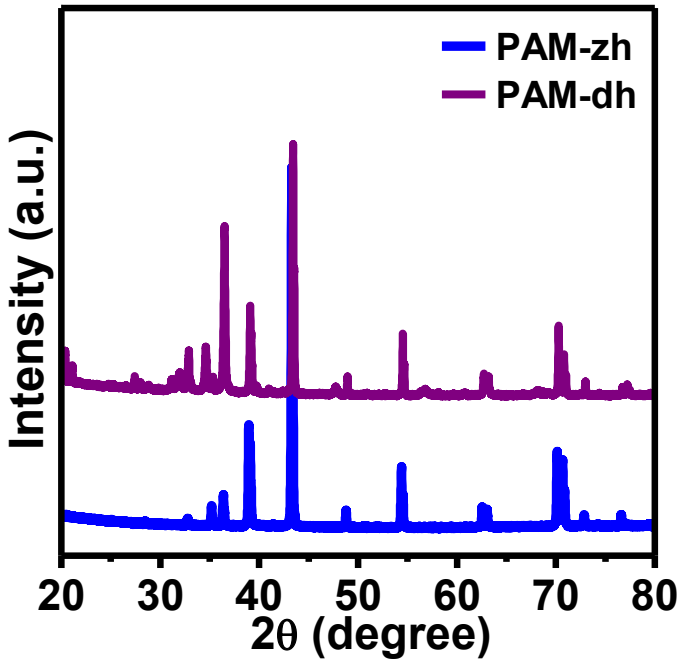

Fig. S31 PXRD of Zn plate after the cycling tests of the symmetric Zn | |Zn cells with PAM-dh and PAM-zh electrolyte at current density 5 mA cm^{-2}.

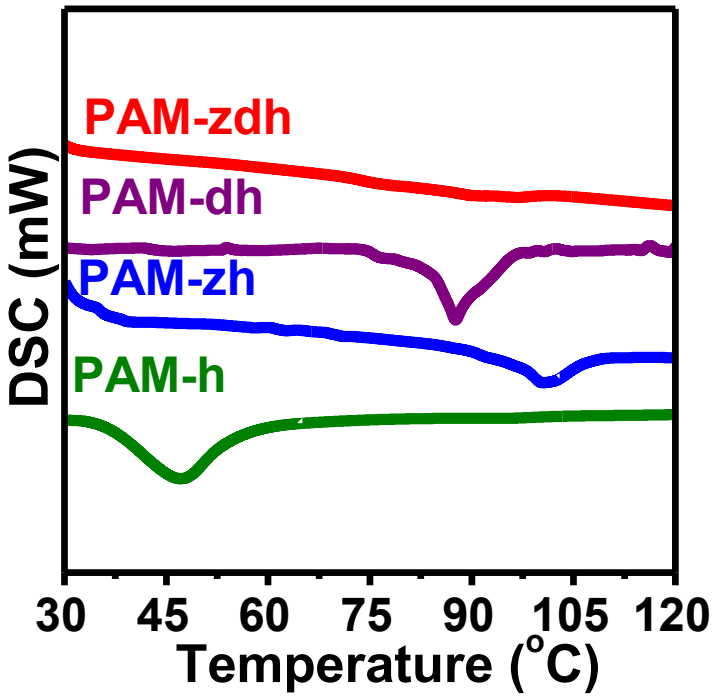

Fig. S32 DSC curves of PAM-h, PAM-dh, PAM-zh, and PAM-zdh.

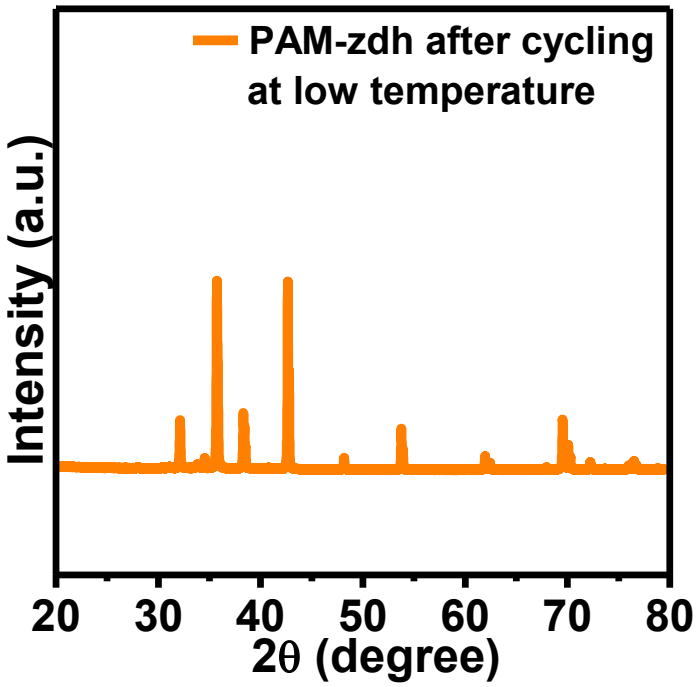

Fig. S33 PXRD of Zn plate after the cycling tests of the symmetric Zn | |Zn cells with PAM-zdh under ice conditions at current density 2 mA cm^{-2}.

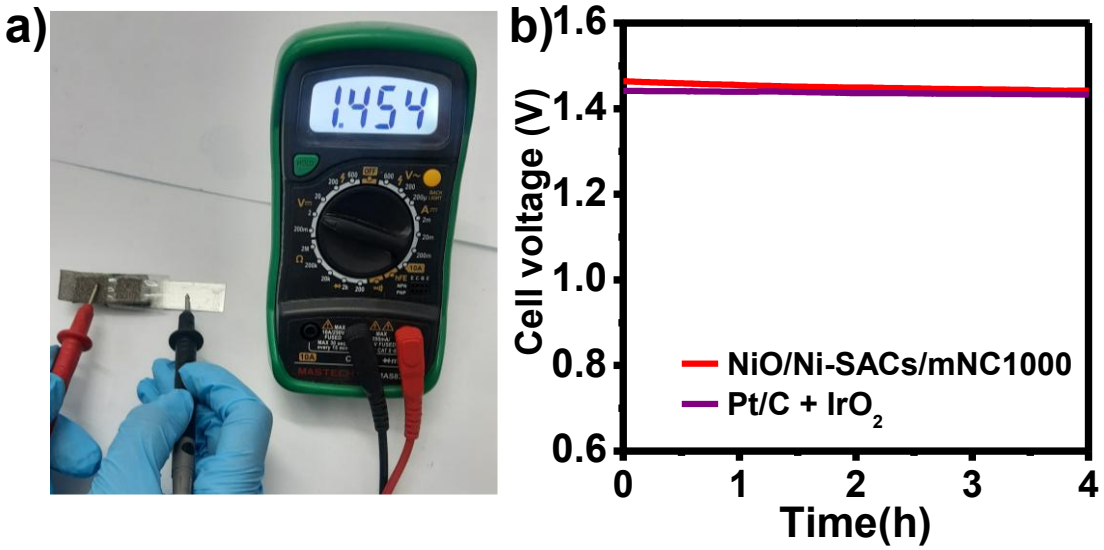

Fig. S34 a) Photograph displaying measured open-circuit voltage of 1.454 V, and b) open circuit voltage of 1.454 and 1.446 V using PAM-zdh electrolyte for NiO/Ni-SACs/mNC1000 and Pt/C+IrO_2 couple, respectively.

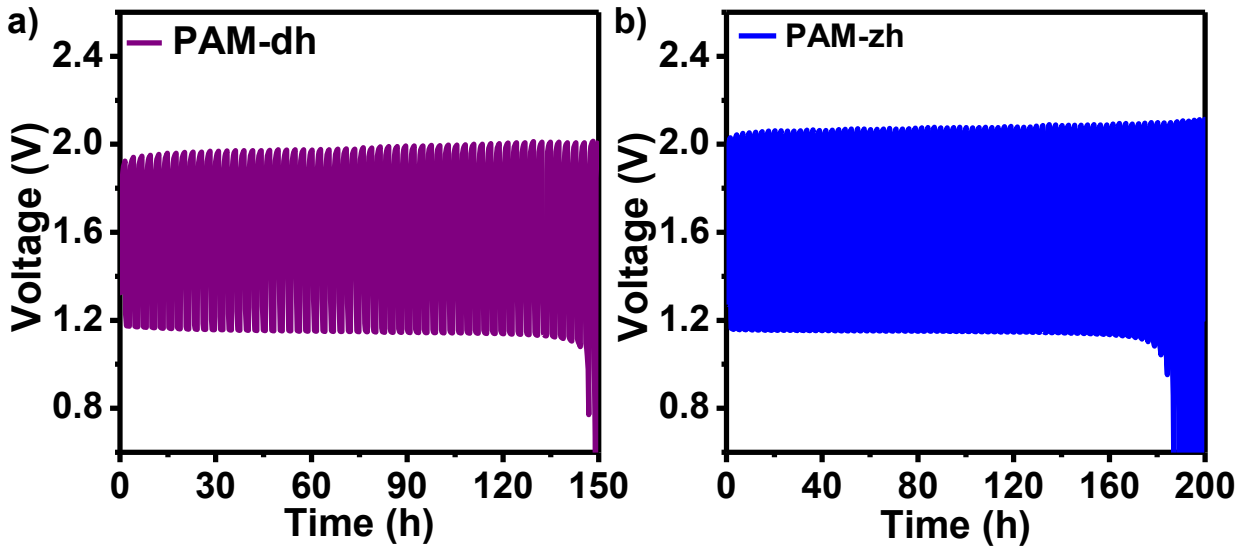

Fig. S35 Charging-discharging test of solid-state ZAB at 20 mA cm^{-2} with different gel electrolytes a) PAM-dh, and b) PAM-zh. In both cases NiO/Ni-SACs/mNC1000 was used as cathode.

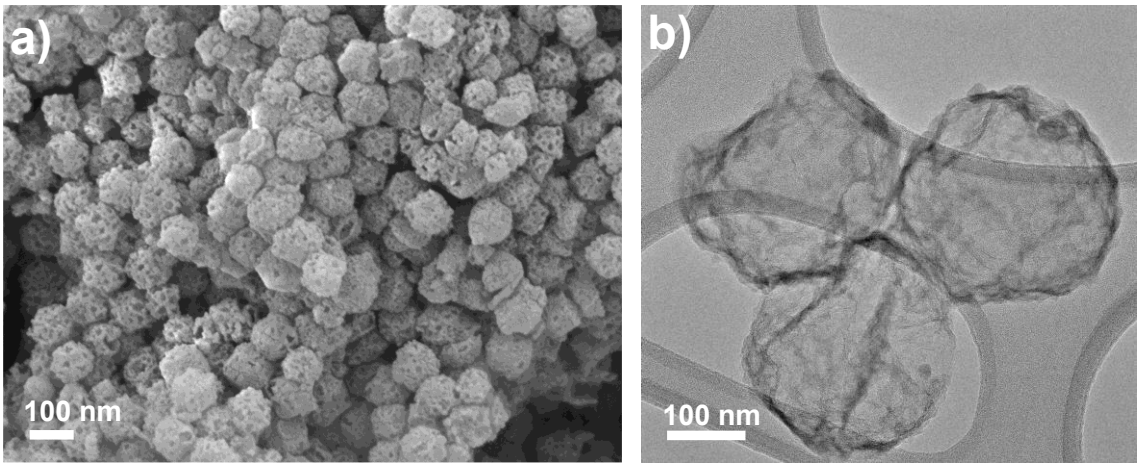

Fig. S36 a) SEM and b) TEM image of NiO/Ni-SACs/mNC1000 after testing in quasi-solid-state ZAB.

Table S4 Performance comparison of quasi-solid-state ZABs at low-temperatures.

Catalysts	Gel Electrolyte Composition	Working Temperature	Battery Cycling Performance	References
NiO/Ni-SACs/mnc-1000	PAM + DMSO + $Zn(BF_4)_2$	-70 °C	~400 h @ 2 mA cm^{-2}	This work
Co SA-NDGs	PAM organohydrogel electrolyte (PAM+ DMSO)	-60 °C	~300 h @ 0.5 mA cm^{-2}	1
Pt/C + Ir/C	CsOH-based electrolyte	-10 °C	~500h @ 5 mA cm^{-2}	2
Pt/RuO_2/CC	PAM-CNF/KOH/KI-based hydrogel	-40 °C	~ 45 h@2 mA cm^{-2}	3
MnFeCoNiRu/ CNF	O-P(AA-co-AM)	-50 °C	~1000 cycles/N (20 min per cycle) @5 mA cm^{-2}	4
FeMn-DSAC	PAM/MMT	-40 °C	~30 h @ 2 mA cm^{-2}	5
Co_9S_8-NSABP	PANa–PVA–IL	-40 ^{0}C	~200 h @ 2 mA cm^{-2}	6
Co_3O_4	PAMPSK25- MC2.0-5M	-20 °C	~24 h @ 2 mA cm^{-2}	7
Co@N-PCP/NBCNF	G–CyBA/PAAm SP-DN	-50 °C	~40 h @ 2 mA cm^{-2}	8
NiO/CoO TINWs	PVA	-10 °C	~14 h @ 2 mA cm^{-2}	9
$Ni_{0.8}Fe_{0.2}$ NSs	PVA	-10 °C	~20 h @ 0.5 mA cm^{-2}	10

References:

[1] Q. Wang, Q. Feng, Y. Lei, L. Xu, Y. Xiong, G. Fang, Y. Wang, P. Yang, J. Liu, W. Liu and X. Xiong, *Nat. Commun*., 2022, **13**, 3689.

[2] C.-X. Zhao, J.-N. Liu, N. Yao, J. Wang, D. Ren, X. Chen, B.-Q. Li and Q. Zhang, *Angew. Chem. Int. Ed.*, 2021, **60**, 15281.

[3] Y. Zhanga, H. Qina, M. Alfreda, H. Ke, Y. Cai, Q. Wang, F. Huang, B. Liu, P. Lv and Q. Wie, *Energy Storage Mater*., 2021, **42**, 88.

[4] T. Gu, Y. Jia, L. Zhang, L. Zhao, J. Shen, L. Ouyang, M. Zhu and J. Liu, *J. Am. Chem. Soc*., 2025, **147**, 15029.

[5] T. Cui, Y.-P. Wang, T. Ye, J. Wu, Z. Chen, J. Li, Y. Lei, D. Wang and Y. Li, *Angew. Chem. Int. Ed.,* 2022, **61**, e202115219.

[6] X. Zhong, Z. Zheng, J. Xu, X. Xiao, C. Sun, M. Zhang, J. Ma, B. Xu, K. Yu, X. Zhang, H.-M. Cheng and G. Zhou, *Adv. Mater*., 2023, **35**, 2209980.

[7] N. Sun, F. Lu, Y. Yu, L. Su, X. Gao and L. Zheng, *ACS Appl. Mater. Interfaces*, 2020, **12**, 11778.

[8] C. Gu, X.-Q. Xie, Y. Liang, J. Li, H. Wang, K. Wang, J. Liu, M. Wang, Y. Zhang, M. Li, H. Kong and C.-S. Liu, *Energy Environ. Sci*., 2021, **14**, 4451.
[9] L. An, B. Huang, Y. Zhang, R. Wang, N. Zhang, T. Dai, P. Xi and C.-H. Yan, *Angew. Chem. Int. Ed.*, 2019, **58**, 9459.
[10] R. Yang, L. An, Y. Zhang, N. Zhang, T. Dai and P. Xi, *ChemCatChem*, 2019, **11**, 6002.